

Anisotropic separate universe simulations

Shogo Masaki^{1,2★}, Takahiro Nishimichi^{3,4} and Masahiro Takada⁴

¹*Department of Mechanical Engineering, National Institute of Technology, Suzuka College, Suzuka, Mie 510-0294, Japan*

²*Department of Physics, Nagoya University, Nagoya, Aichi 464-8601, Japan*

³*Center for Gravitational Physics, Yukawa Institute for Theoretical Physics, Kyoto University, Kyoto 606-8502, Japan*

⁴*Kavli Institute for the Physics and Mathematics of the Universe (WPI), The University of Tokyo Institutes for Advanced Study (UTIAS), The University of Tokyo, Kashiwa, Chiba 277-8583, Japan*

4 January 2022

ABSTRACT

The long-wavelength coherent overdensity and tidal force, which are not direct observables for a finite-volume survey, affect time evolution of cosmic structure formation and therefore clustering observables through the mode coupling. In this paper we develop an “anisotropic” separate universe (SU) simulation technique to simulate large-scale structure formation taking into account the effect of large-scale tidal force into the anisotropic expansion of local background. We modify the TreePM N -body simulation code to implement the anisotropic SU simulations, and then study the “response” function of matter power spectrum that describes how the matter power spectrum responds to the large-scale tidal effect as a function of wavenumber and redshift for a given global cosmology. We test and validate the SU simulation results from the comparison with the perturbation theory predictions and the results from high-resolution PM simulations. We find that the response function displays characteristic scale dependences over the range of scales down to nonlinear scales, up to $k \simeq 6 h \text{ Mpc}^{-1}$.

Key words: large-scale structure of Universe – cosmology: theory

1 INTRODUCTION

Large-scale structure of the universe is now recognized as a powerful probe of cosmology as it enables us to constrain properties of primordial fluctuations, explore the nature of dark matter and dark energy, and obtain precise measurements of cosmological parameters. For this reason, there are various ongoing and planned wide-area galaxy surveys such as the Subaru Hyper Suprime-Cam survey (Aihara et al. 2018), the Subaru Prime Focus Spectrograph (PFS) survey (Takada et al. 2014), the ESA Euclid mission (Laureijs et al. 2011), the Legacy Survey of Space and Time¹, and the NASA WFIRST mission (Spergel et al. 2015).

To attain the full potential of such wide-area galaxy surveys, there are both observational and theoretical challenges. On observation side we need high-precision characterization and measurements of the statistical properties of large-scale structure. On theory side we need accurate theoretical templates of the clustering observables to compare with the high-precision measurements at scales down to the nonlinear regime. However, there are unavoidable uncertainties in the large-scale structure cosmology. Such an example is the uncertainties arising from “super-sample” modes

(Takada & Hu 2013) that are the effects of fluctuations with wavelengths comparable with or greater than a size of survey volume. Super-sample modes are not direct observables for a finite-volume survey, but affect the time evolution of sub-survey modes and therefore clustering observables through the nonlinear mode coupling (Hamilton et al. 2006; Sato et al. 2009; Takada & Hu 2013). The super-sample effects are also not easy to theoretically study, because N -body simulations, which are standard tools to study nonlinear structure formation, usually employ the periodic boundary conditions and ignore the effects of super-box modes (Sirko 2005; Gnedin et al. 2011).

There are two super-sample effects that are both related to the Hessian tensor of the long-wavelength gravitational potential and therefore of equal importance. The first is the coherent density contrast, and the effects on various clustering observables have been well studied using the perturbation theory and N -body simulations (Sirko 2005; Takada & Jain 2009; Baldauf et al. 2011; Sherwin & Zaldarriaga 2012; Takada & Hu 2013; Kayo et al. 2013; Li et al. 2014a; Mohammed et al. 2014; Wagner et al. 2015a,b; Baldauf et al. 2016; Barreira et al. 2018; Takahashi et al. 2019; Barreira et al. 2019). In particular, the effects can be absorbed into a change of cosmological parameters, especially the spatial curvature, in an isotropic Friedmann-Robertson-Walker (FRW) background. Hence we can run N -body sim-

★ shogo.masaki@gmail.com

¹ <https://www.lsst.org>

ulations in the modified FRW background to fully study the super-sample effects over all scales down to the deeply nonlinear regime – so-called separate universe (SU) simulation technique (Li et al. 2014a; Wagner et al. 2015a; Baldauf et al. 2016). The SU simulations allow for an accurate calibration of the super-sample effects on desired observables, because paired SU simulations using the same seeds of initial conditions significantly reduce the sample variance errors in simulations.

Another super-sample effect arises from the large-scale tidal force. The tidal effect causes an apparent anisotropic clustering in the large-scale structure depending on the degree of alignments between the wavevector and the tidal tensor in a given survey realization (Schmidt & Jeong 2012; Dai et al. 2015; Ip & Schmidt 2017; Akitsu et al. 2017; Akitsu & Takada 2018; Li et al. 2018; Akitsu et al. 2019). Most of the previous studies were based on the perturbation theory. One difficulty for a simulation based study is the large-scale tidal force cannot, by definition, be absorbed by a modification of an isotropic FRW background cosmology. Instead one needs to consider an “anisotropic” expansion to include the tidal effect into the local background, which we call an anisotropic SU simulation approach. Schmidt et al. (2018) made the first attempt to develop the anisotropic SU simulation technique, using the PM method.

Hence the purpose of this paper is to develop the anisotropic SU simulation technique by modifying the TreePM algorithm in the publicly-available GADGET-2 code (Springel 2005). The TreePM, in which the tree force complements the poor accuracy of the PM force near and below the mesh size, is one of the most powerful numerical method to simulate nonlinear structure formation including formation and properties of halos where galaxies and galaxy clusters form. Then we use the SU simulations to study the “response” function of matter power spectrum that describes how the large-scale tidal force affects the matter power spectrum as a function of wavenumber and redshift for a given global cosmology.

The rest of this paper is structured as follows. Section 2 presents a formulation for anisotropic SU simulations based on the TreePM method. After deriving the response function of the matter power spectrum to the large-scale tidal force in Section 3, we study the response function using the SU simulations in Sections 4 and 5, where we also give a validation of the SU simulations from the comparison with the perturbation theory prediction and with the high-resolution PM simulations. Section 6 is devoted to conclusion and discussion. Throughout this paper we consider the standard Λ and cold dark matter dominated cosmology with adiabatic Gaussian initial conditions (Λ CDM).

2 ALGORITHM OF SEPARATE UNIVERSE SIMULATION INCLUDING LARGE-SCALE TIDAL EFFECT

The purpose of this paper is to modify the publicly-available N -body code, GADGET-2 (Springel et al. 2001; Springel 2005), to include the effect of super-box tidal force on large-scale structure formation simulated in an N -body simulation of a finite volume – so-called separate universe (SU) simulation. In this section, we present a formulation needed for the

modification of the N -body code. We first briefly review the formulation for a standard N -body code, i.e. N -body simulations in an isotropic, homogeneous Friedmann-Robertson-Walker (FRW) background, and then present a formulation for the N -body code in SU simulations we employ in this paper. Our formulation is based on the concept illustrated in Figure 1.

2.1 Preliminaries: Newtonian N -body simulation equations in an isotropic FRW background

We begin by briefly reviewing basic equations used in standard N -body simulations in an isotropic, homogeneous FRW background. We also define notations of quantities used in this paper. To consider structure formation in an expanding FRW background, it is quite convenient to consider the gravitational evolution in the *comoving* coordinate, where an isotropic, homogeneous FRW expansion is solved separately, and the background equations are subtracted from a set of dynamical equations that govern structure formation including time evolution of density fluctuations. The comoving coordinate, denoted by \mathbf{x} , is related to the physical coordinate, denoted by \mathbf{r} , via

$$\mathbf{r} = a(t)\mathbf{x}, \quad (1)$$

where $a(t)$ is the scale factor that describes an expansion history of the FRW background. The time evolution of $a(t)$ in a matter dominated era is governed by the Einstein equation, the so-called Friedmann equation:

$$\frac{\ddot{a}}{a} = -\frac{4\pi G\bar{\rho}(t)}{3} + \frac{\Lambda}{3}, \quad (2)$$

where the dot notation $\dot{}$ denotes the time derivative, $\bar{\rho}(t)$ is the mean matter density, given by $\bar{\rho}(t) = \bar{\rho}_0/a(t)^3$, $\bar{\rho}_0$ is the present-day matter density, and Λ is the cosmological constant. The cosmological parameters are often used to specify $\bar{\rho}_0$ and Λ as $\bar{\rho}_0 = \Omega_{\text{m}0}\bar{\rho}_{\text{cr}0}$ and $\Lambda = 8\pi G\Omega_{\Lambda}\bar{\rho}_{\text{cr}0}$, where $\bar{\rho}_{\text{cr}0}$ is the critical density, defined as $\rho_{\text{cr}0} \equiv 3H_0^2/8\pi G \approx 1.88 \times 10^{-29} h^2 \text{g cm}^{-3}$, for the convention of $c = 1$ for the speed of light. Throughout this paper we consider a flat-geometry universe: $\Omega_{\text{m}0} + \Omega_{\Lambda} = 1$.

When the matter distribution has initial perturbations as predicted in the standard structure formation scenario, the spatial inhomogeneities grow due to the gravitational instability (Peebles 1980; Dodelson 2003). Following the convention in Springel et al. (2001), we use a normalized peculiar velocity, corresponding to the canonical momentum:

$$\mathbf{u} \equiv a^2\dot{\mathbf{x}}. \quad (3)$$

Given this definition, we can introduce the effective Newtonian gravitational potential including the contribution of the cosmological constant, via the Poisson equation in the physical coordinate:

$$\nabla_{\mathbf{r}}^2\phi(\mathbf{r}; t) = 4\pi G\rho(\mathbf{r}; t) - \Lambda, \quad (4)$$

where $\rho(\mathbf{r}; t)$ is the total matter density field and can be expressed in terms of the mean matter density ($\bar{\rho}$) and the matter density fluctuation field $\delta(\mathbf{r}; t)$ as $\rho(\mathbf{r}; t) \equiv \bar{\rho}(t)[1 + \delta(\mathbf{r}; t)]$. The equation of motion for a test particle is given by

$$\ddot{\mathbf{r}} = -\nabla_{\mathbf{r}}\phi = -\frac{1}{a}\nabla_{\mathbf{x}}\phi. \quad (5)$$

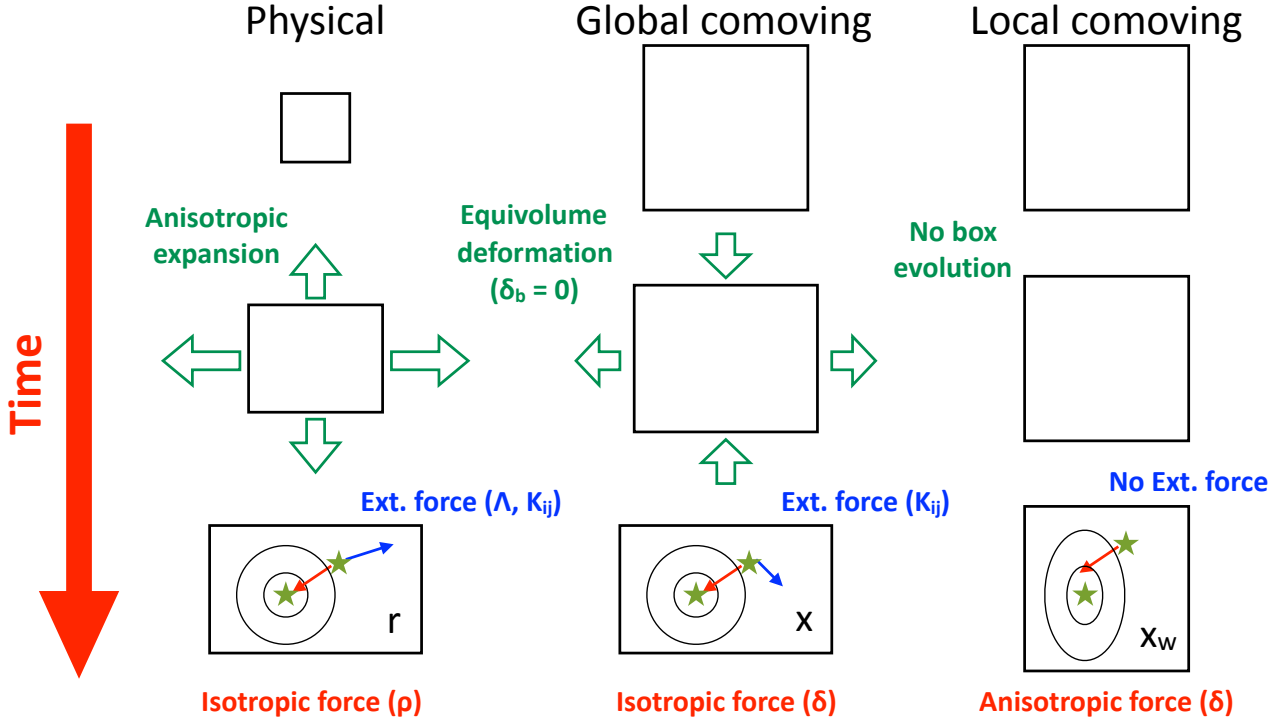


Figure 1. A schematic illustration of structure formation in a finite volume region with the large-scale tidal field in different coordinate systems. The boundary box denotes the Lagrangian volume at the initial epoch (upper panels), and we show how the volume in different coordinates evolves with time. The circular lines in the bottom panels depict iso-amplitude contours of the gravitational potential that is induced by a star-symbol particle at the center of the circle (ellipsoid). Then we consider the gravitational force acting on a test particle denoted by another star symbol. *Left:* The physical coordinate. The total gravitational force is given by a sum of the two contributions; the external gravitational force that arises from the spatially-homogeneous parts (the cosmological constant and the super-survey tidal tensor $K_{ij}(t)$), denoted by the blue arrow, and the gravitational force from the particle at the center, denoted by the red arrow. *Middle:* The standard comoving coordinate (the global comoving coordinate). The gravitational force corresponding to the isotropic expansion due to the mean matter density and the cosmological constant can be absorbed into the scale factor, $a(t)$, whose time evolution is given by the Friedmann equation. Then the gravitational force due to the super-survey tidal tensor needs to be given as an external force (blue arrow). The force from the mass overdensity with respect to the mean density (δ) due to the particle at the center is denoted by the red arrow. Here we consider the region with the same volume as that in the physical coordinate at a target redshift (bottom panels). *Right:* The comoving coordinate in the SU simulation (the local comoving coordinate). Now the force due to the super-survey tidal tensor (K_{ij}) is further absorbed into the comoving scale factor, $a_{W_i}(t)$. In this case the background has an anisotropic expansion. The gravitational force from the particle at the center becomes anisotropic: the force direction deviates from the direction connecting the two particles. The simulation volume in the SU comoving coordinate appears to stay the same. We have to design the SU simulation so that the time evolution of self-gravitating system should be equivalent to those in the physical or global comoving coordinates.

On the other hand, the second time derivative of Eq. (1) yields

$$\ddot{\mathbf{r}} = \ddot{a}\mathbf{x} + 2\dot{a}\dot{\mathbf{x}} + a\ddot{\mathbf{x}}. \quad (6)$$

Using Eqs. (3) and (5), we can rewrite the equation of motion as

$$\ddot{\mathbf{u}} = -\nabla_{\mathbf{x}}\phi - a\ddot{a}\mathbf{x} \equiv -\frac{1}{a}\nabla_{\mathbf{x}}\Phi. \quad (7)$$

In the last equality on the r.h.s., we introduced the ‘‘peculiar’’

gravitational potential defined by

$$\Phi \equiv a \left[\phi + \frac{1}{2}a\ddot{a}x^2 \right]. \quad (8)$$

Using Eqs. (2) and (4), we can find that the peculiar gravitational potential obeys the Poisson equation in the comoving coordinate:

$$\nabla_{\mathbf{x}}^2\Phi(\mathbf{x}; t) = 4\pi G\bar{\rho}_0\delta(\mathbf{x}; t). \quad (9)$$

The use of the peculiar gravitational potential is convenient, because it arises from the density fluctuation field which is a spatially varying field, $\delta(\mathbf{x}, t)$. Even if the gravitational force

in the physical coordinate has source terms arising from the mean matter density and the cosmological constant (Eq. 4), the force contributions can be absorbed into the effect on the scale factor via the Friedmann equation. The development of SU simulation for the large-scale tidal effect is based on the similar concept, as we discuss below (see Figure 1).

To perform a fast computation of the peculiar gravitational force and increase the dynamic ranges, we approximate the gravity force by a sum of the two parts that are computed based on the particle-mesh (PM) method and the tree algorithm – the so-called TreePM code (Xu 1995; Bode et al. 2000; Bagla 2002),

$$\Phi(\mathbf{x}; t) \simeq \Phi^{\text{PM}}(\mathbf{x}; t) + \Phi^{\text{T}}(\mathbf{x}; t). \quad (10)$$

Here the PM part computes the gravitational force on large scales treating a system of N -body particles as a coarse-grained fluid, while the tree part computes the direct gravitational force between N -body particles on small scales. The division is to some extent arbitrary, and the parameters to determine the division need to be carefully tested and calibrated. When we include the effect of large-scale tidal force, we need to carefully study whether the division in a SU simulation causes an artifact, which is one of the main purposes of this paper.

For the PM force calculation, it is useful to use the fast Fourier transform (FFT) method that allows for a fast computation of the gravitational field if grid-based data is given. From Eq. (9), the Fourier transform of the gravitational field is given by

$$\tilde{\Phi}_{\mathbf{k}}^{\text{PM}} = -\frac{4\pi G \bar{\rho}_0 \tilde{\delta}_{\mathbf{k}}}{k^2} = -4\pi G \bar{\rho}_0 \tilde{\delta}_{\mathbf{k}} G(k), \quad (11)$$

where $k^2 \equiv \sum_i (k_i)^2$, $G(k) \equiv 1/k^2$ is the Green function and $\tilde{\delta}_{\mathbf{k}}$ is the Fourier transformed density fluctuation. Fourier-transforming $\tilde{\Phi}_{\mathbf{k}}^{\text{PM}}$ back to real space gives the gravitational field due to the density field smoothed over the Fourier grids. Here the number of FFT grids determines the resolution of the FFT based gravitational force for a given simulation box size; if we employ N_{grid} grids, the PM gravitational force is accurate on larger scales, $x \gg L_{\text{box}}/N_{\text{grid}}^{1/3}$ or $k \ll N_{\text{grid}}^{1/3} k_{\text{f}}$, where k_{f} is the fundamental Fourier mode, $k_{\text{f}} = 2\pi/L_{\text{box}}$ (L_{box} is a size of N -body simulation box on a side). For the FFT computation we need to define the grid-based data from the distribution of N -body particles, and we adopt the Cloud in Cell (CIC) interpolation scheme in this paper. Consistently, the force interpolation from grid points is done with the same CIC algorithm. Following the original implementation of GADGET-2, we divide the potential field by the square of the CIC kernel in Fourier space to account for the two interpolation steps together with the multiplication of the Green function described below. We, however, omit the window function from the equations in what follows for notational simplicity. What is important in this process is that the FFT method implicitly assumes the periodic boundary conditions of the data. While this is advantageous in the sense that it automatically takes into account the force from infinite mirror images of the simulation box, the method ignores the effect of super-box modes with $k < k_{\text{f}}$ by construction. Another advantage of the PM method is that, as long as we can increase N_{grid} or equivalently the Fourier resolution for a fixed simulation box size, the gravity is very accurately simulated at scales greater than the FFT limit.

Hence we can use the PM results with high resolution to test the TreePM method for the SU simulations. Finally, to leave gravity in short ranges to the Tree algorithm, the PM potential in the Fourier space needs to be smoothly truncated around FFT grid scales, which is done by the split factor:

$$\tilde{\Phi}_{\mathbf{k}}^{\text{PM}} \rightarrow \tilde{\Phi}_{\mathbf{k}}^{\text{PM}} \exp\left(-k^2 x_{\text{s}}^2\right), \quad (12)$$

where x_{s} is the comoving split scale. For our computation, we set $x_{\text{s}} = 4.5 L_{\text{box}}/N_{\text{grid}}^{1/3}$.

On the other hand, the gravitational potential in short ranges is computed based on the Tree algorithm. The gravitational potential at the position of the n -th N -body particle is computed from a direction summation of the $1/r$ -force between N -body particles:

$$\Phi^{\text{T}}(\mathbf{x}_n) = -Gm \sum_{n':n' \neq n} \frac{1}{|\mathbf{x}_n - \mathbf{x}_{n'}|} \text{erfc}\left(\frac{|\mathbf{x}_n - \mathbf{x}_{n'}|}{2x_{\text{s}}}\right), \quad (13)$$

where the summation runs over all the n' -th particles except the n -th particle (i.e. $n' \neq n$), m is the particle mass, and $\text{erfc}(x)$ is the complementary error function. The factor with erfc is the split factor for the Tree force; the gravitational force contribution from the n' -th particle in large distances $|\mathbf{x}_n - \mathbf{x}_{n'}| \gg x_{\text{s}}$ is suppressed because $\text{erfc}(x) \simeq 0$ for $x \gg 1$. Note that the contribution from the mean density should be subtracted from this expression because it is already absorbed into the coordinate transformation. However, with the periodic boundary condition employed in the simulations, this does not affect the motion of simulation particles at all. In an isotropic universe background, the resultant Tree gravitational acceleration is

$$-\nabla_{\mathbf{x}} \Phi^{\text{T}}(\mathbf{x}_n) = -Gm \sum_{n':n' \neq n} \frac{\mathbf{x}_n - \mathbf{x}_{n'}}{|\mathbf{x}_n - \mathbf{x}_{n'}|^3} \times \left[\text{erfc}\left(\frac{|\mathbf{x}_n - \mathbf{x}_{n'}|}{2x_{\text{s}}}\right) + \frac{|\mathbf{x}_n - \mathbf{x}_{n'}|}{x_{\text{s}} \sqrt{\pi}} \exp\left(-\frac{|\mathbf{x}_n - \mathbf{x}_{n'}|^2}{4x_{\text{s}}^2}\right) \right]. \quad (14)$$

The factor of $(-1/|\mathbf{x}_n - \mathbf{x}_{n'}|)$ in Eq. (13) is replaced with a kernel incorporating the softening length to avoid gravity divergence (Springel et al. 2001). In GADGET-2, the gravitational potential for a group of particles is expanded in multipole series, and the gravitational force is calculated only with the monopole term (Springel 2005). Together with the split factor, the final Tree acceleration form is

$$-\nabla_{\mathbf{x}} \Phi^{\text{T}}(\mathbf{x}_n) = G \sum_{\text{group}} M_{\text{group}} g_1(y_{\text{group}}) \mathbf{y}_{\text{group}} \times \left[\text{erfc}\left(\frac{y_{\text{group}}}{2x_{\text{s}}}\right) + \frac{y_{\text{group}}}{x_{\text{s}} \sqrt{\pi}} \exp\left(-\frac{y_{\text{group}}^2}{4x_{\text{s}}^2}\right) \right], \quad (15)$$

where $\mathbf{y}_{\text{group}} = \mathbf{x}_n - \mathbf{s}_{\text{group}}$, $\mathbf{s}_{\text{group}}$ is the center-of-mass of the particle group with the total mass M_{group} and g_1 is the monopole term of the potential expanded in the multipole series (Springel et al. 2001). In the summation above, since the Tree force is confined to small scales, we need to consider only the nearest image out of the infinite periodic mirrors.

The ‘‘peculiar’’ Hamiltonian for a system of N -body particles is

$$H = \sum_n \frac{\mathbf{p}_n^2}{2ma^2} + \frac{1}{2} \sum_n \frac{m\Phi(\mathbf{x}_n)}{a}, \quad (16)$$

where the first term is the kinetic energy with the canonical momentum defined by $\mathbf{p} = m\mathbf{u}$ and the second term is

the gravitational potential arising from the inhomogeneous distribution of N -body particles (that is, the homogeneous parts such as $\bar{\rho}$ and Λ are implicitly included only in the time evolution of the scale factor a in this Hamiltonian). GADGET-2 employs the time-evolution operators for the kinetic and the potential parts of the Hamiltonian (Quinn et al. 1997; Springel 2005):

$$D(\Delta t) : \begin{cases} \mathbf{p}_n \rightarrow \mathbf{p}_n \\ \mathbf{x}_n \rightarrow \mathbf{x}_n + \frac{\mathbf{p}_n}{m} \int_t^{t+\Delta t} a^{-2} dt \end{cases}, \quad (17)$$

$$K(\Delta t) : \begin{cases} \mathbf{p}_n \rightarrow \mathbf{p}_n + \mathbf{f}_n \int_t^{t+\Delta t} a^{-1} dt \\ \mathbf{x}_n \rightarrow \mathbf{x}_n \end{cases}, \quad (18)$$

where $\mathbf{f}_n = -m\nabla_{\mathbf{x}}\Phi(\mathbf{x}_n)$. The factors $I_{\text{drift}} = \int_t^{t+\Delta t} a^{-2} dt$ and $I_{\text{kick}} = \int_t^{t+\Delta t} a^{-1} dt$ are called the drift and kick factors, respectively.

2.2 SU simulation including large-scale tidal effect in an anisotropic expanding background

The SU simulation technique is a useful way to include the effect of super-box density fluctuations on cosmic structure formation in an N -body simulation (Bond & Myers 1996; Sirko 2005; Gnedin et al. 2011; Li et al. 2014a; Wagner et al. 2015a; Baldauf et al. 2016; Schmidt et al. 2018). In this method, we can absorb the effect of large-scale gravitational force into the background metric by modifying the scale factor as illustrated in Figure 1.

We begin with a brief review of the concept behind the SU simulation (Takada & Hu 2013; Akitsu et al. 2017). We first consider the gravitational field smoothed by a survey window W , $\Psi^L(\mathbf{x})$, where the superscript “ L ” denotes that the gravitational field arises from the long-wavelength density fluctuations with scales comparable with or greater than a size of the survey window. Here we also introduce the peculiar gravitational potential Ψ obeying the Poisson equation, $\nabla_{\mathbf{x}}^2\Psi = 4\pi G\bar{\rho}a^2\delta(\mathbf{x}, t)$, and note that this is different from the definition of the peculiar gravitational potential defined by Eq. (9) via $\Phi = a\Psi$. Taylor-expanding the gravitational field around the position of \mathbf{x}_0 (e.g. the center of the survey volume), we have

$$\Psi^L(\mathbf{x}) = \Psi^L(\mathbf{x}_0) + \nabla_i\Psi^L|_{\mathbf{x}_0}\Delta x^i + \frac{1}{2}\nabla_i\nabla_j\Psi^L|_{\mathbf{x}_0}\Delta x^i\Delta x^j + \mathcal{O}(\nabla^3\Psi^L|_{\mathbf{x}_0}\Delta x^3) \quad (19)$$

where $\Delta x^i = (\mathbf{x} - \mathbf{x}_0)^i$, $\nabla_i = \partial/\partial x_i$. The superscript “ L ” denotes the gravitational potential that arises from the super-survey modes. Without loss of generality we can decompose the second derivative tensor into two independent modes, the trace part and the trace-less tensor part as

$$\nabla_i\nabla_j\Psi^L|_{\mathbf{x}_0} = 4\pi G\bar{\rho}a^2\left(\frac{1}{3}\delta_{ij}^K\delta_b + K_{ij}\right), \quad (20)$$

where

$$\delta_b \equiv \frac{1}{4\pi G\bar{\rho}a^2} \nabla^2\Psi^L|_{\mathbf{x}_0} \quad (21)$$

$$K_{ij} \equiv \frac{1}{4\pi G\bar{\rho}a^2} \left(\nabla_i\nabla_j\Psi^L - \frac{1}{3}\delta_{ij}^K\nabla^2\Psi^L \right) \Big|_{\mathbf{x}_0}, \quad (22)$$

δ_{ij}^K is the Kronecker delta function, δ_b is the density contrast (DC mode) in the survey window and K_{ij} is the super-survey tidal tensor satisfying the trace-less condition, $\text{Tr}(K_{ij}) = 0$. As can be found from the above equation, $K_{ij}(t) \propto D_+(t)$, where $D_+(t)$ is the linear growth factor, if a survey volume is sufficiently large and in this case the gravitational field Ψ^L is safely considered to be in the linear regime. Since δ_b and K_{ij} are independent in the linear regime, we consider $\delta_b = 0$ throughout this paper.

For a particular realization of a sufficiently large-volume galaxy survey, the large-scale tidal tensor is only a temporal function, $K_{ij} = K_{ij}(t)$, evolving according to the linear growth rate, and the amplitude is randomly drawn from the Gaussian statistics of survey scale in the adiabatic Gaussian initial conditions in the standard Λ CDM model. As discussed in Akitsu et al. (2017), the effect of K_{ij} can be absorbed by modifying the background expansion of the local realization. However, to do this, we need to consider an anisotropic expansion for the local background, because the effect is anisotropic by definition, and cannot be absorbed by modifying an isotropic FRW background, unlike the effect of large-scale density contrast, δ_b (Li et al. 2014a). Without loss of generality we can take the coordinate system whose axes are along the principal axes of the large-scale tidal tensor, K_{ij} . In this coordinate system, the tensor K_{ij} becomes diagonal: $K_{ij} = K_i\delta_{ij}^K$, where K_i is the eigenvalues along each axis and the traceless condition reads $\sum_i K_i = 0$. Using the Zel’dovich approximation (Zel’dovich 1970) (also see Bond & Myers 1996; Akitsu et al. 2017; Akitsu & Takada 2018), we introduce the anisotropic scale factor along each coordinate axis, denoted as $a_{W_i}(t)$:

$$a_{W_i}(t) \simeq a(t)[1 - K_i(t)] \equiv a(t)\alpha_{W_i}(t) \quad (23)$$

where $a(t)$ is the scale factor of the global background and obeys the original Friedmann equation (Eq. 2). Hereafter quantities with subscript “ W ” denote their quantities in the local background or the comoving coordinate of SU simulation as defined below. $\alpha_{W_i}(t)$ is the normalized anisotropic scale factor, defined as $\alpha_{W_i}(t) \equiv a_{W_i}(t)/a(t)$, satisfying the condition, $\sum_i \alpha_{W_i} = 3$. For a sufficiently high redshift, $\alpha_{W_i}(t) \rightarrow a(t)$ due to $K_i(t) \rightarrow 0$. We use the code to calculate α_{W_i} for a general case following the method in Schmidt et al. (2018) (see Section 2 in their paper).

For a sufficiently large volume, the large-scale tidal force is safely in the linear regime. We introduce three constants, λ_i ($i = 1, 2, 3$), to parameterize the normalization of large-scale tidal tensor as

$$K_i(t) = D_+(t)\lambda_i. \quad (24)$$

The traceless nature of K_{ij} leads to $\sum_i \lambda_i = 0$. λ_i can be considered as normalization parameters of the large-scale tidal tensor today as we adopt the normalization given by $D_+(t_0) = 1$ today.

Whilst the physical coordinate should be invariant, the comoving coordinate in the local background needs to be modified, if the local scale factor a_W is introduced:

$$r_i = a_{W_i}(t)x_{W_i}, \quad (25)$$

where x_{W_i} is the comoving coordinate component in the local coordinate to which we will simply refer as “local comoving coordinate”. The local comoving coordinate is different from the comoving coordinate in the global background,

simply “global comoving coordinate”. For a sufficiently high redshift, $r_i = a_{W_i}(t)x_{W_i} \rightarrow a(t)x_{W_i} \rightarrow a(t)x_i$. That is, the local comoving coordinate coincides with the global comoving coordinate (x_i); $x_{W_i} = x_i$ at a sufficiently high redshift, which gives the Lagrangian coordinate condition. Accordingly Eq. (25) means that the comoving wavenumber in the local coordinate is modified as

$$k_{W_i} = \frac{a_{W_{ij}}}{a} k_j \simeq \left(\delta_{ij}^K - K_{ij} \right) k_j = (1 - K_i) k_i = \alpha_{W_i} k_i, \quad (26)$$

where we used the diagonal condition of K_{ij} , $K_{ij} = K_i \delta_{ij}^K$. Note that the notation $\alpha_{W_i} k_i$ does not take the summation over i . In the following, we explicitly use the notation \sum_i to mean the summation. Throughout this paper, we employ the “growth-dilation” technique to run the SU simulation in the local background with anisotropic expansion (see Section III C in Li et al. 2014a, for the isotropic SU simulation case). In this technique, the SU simulation allows us to numerically compute the effect of the super-survey modes on the “growth” of sub-box modes even in a finite-volume simulation. Then the effect of a modification in the comoving coordinate, x_{W_i} , compared to x_i , can be taken into account separately (see below for details).

In the local background, it is convenient to introduce a normalized velocity corresponding to the canonical momentum as

$$u_{W_i} = a_{W_i}^2 \dot{x}_{W_i}. \quad (27)$$

In addition to the Newtonian potential ϕ sourced by the mass density field $\rho(\mathbf{x}; t)$ (Eq. 5), we account for the effect of large-scale tidal force by introducing the external gravitational potential, denoted as $\phi_{W_{\text{ext}}}(\mathbf{r}; t)$:

$$\phi_{W_{\text{ext}}}(\mathbf{r}; t) \equiv 2\pi G \bar{\rho}(t) D_+(t) \sum_i \lambda_i r_i^2. \quad (28)$$

The gravitational force arising from this potential is given as

$$-\partial_{r_i} \phi_{W_{\text{ext}}} = -4\pi G \bar{\rho}(t) D_+(t) \lambda_i r_i. \quad (29)$$

Furthermore, the traceless condition, $\sum_i \lambda_i = 0$, reads

$$\nabla_{\mathbf{r}}^2 \phi_{W_{\text{ext}}} = 0. \quad (30)$$

Thus, denoting the sum of the two potentials as $\phi_{\text{tot}} = \phi + \phi_{W_{\text{ext}}}$, the total potential still obeys the same Poisson equation:

$$\nabla_{\mathbf{r}}^2 \phi_{\text{tot}}(\mathbf{r}) = 4\pi G \rho(\mathbf{r}) - \Lambda. \quad (31)$$

In the presence of the large-scale tide, the mean mass density is given by

$$\begin{aligned} \bar{\rho}_W(t) &\equiv \frac{\bar{\rho}_0}{[a_{W_1} a_{W_2} a_{W_3}](t)} \\ &\simeq \frac{\bar{\rho}_0}{a(t)^3 \left[1 - D_+ \sum_i \lambda_i + O((D_+ \lambda_i)^2) \right]} \\ &= \frac{\bar{\rho}_0}{a(t)^3 \left[1 + O((D_+ \lambda_i)^2) \right]}. \end{aligned} \quad (32)$$

For a sufficiently high redshift, $\bar{\rho}_W(t) \simeq \bar{\rho}_0/a(t)^3$ because $D(t)\lambda_i \rightarrow 0$ and there $a_{W_i}(t) \simeq a(t)$. Note that $\bar{\rho}_W(t) \neq \bar{\rho}(t)$ at the order $O((D_+ \lambda_i)^2)$.

Consider a test particle that rests in the local comoving

coordinate. As $\dot{x}_{W_i} = 0$ for such a particle, the acceleration of the particle is computed as

$$\ddot{r}_i = \ddot{a}_{W_i} x_{W_i}. \quad (33)$$

The gravitational force on this particle can be computed as a sum of the gravitational force arising from the spatially-homogeneous parts, i.e. the mean mass density ($\bar{\rho}$), the cosmological constant (Λ) and the large-scale tidal tensor (K_{ij} or $D_+ \lambda_i$):

$$\begin{aligned} \ddot{r}_i &= -\nabla_{\mathbf{r}} \bar{\phi} - \nabla_{\mathbf{r}} \phi_{W_{\text{ext}}}. \\ &= \left[-\frac{4\pi G \bar{\rho}_W(t)}{3} + \frac{\Lambda}{3} - 4\pi G \bar{\rho}(t) D_+(t) \lambda_i \right] r_i. \end{aligned} \quad (34)$$

Thus, very similarly to the isotropic expanding background in the Λ CDM model, we can account for this homogeneous gravitational force by introducing the scale factor in the local background obeying the following time-differential equation (Figure 1):

$$\frac{\ddot{r}_i}{r_i} = \frac{\ddot{a}_{W_i}}{a_{W_i}} = -\frac{4\pi G \bar{\rho}_W(t)}{3} + \frac{\Lambda}{3} - 4\pi G \bar{\rho}(t) D_+(t) \lambda_i. \quad (35)$$

This is an effective Friedmann equation to describe an anisotropic expansion due to the large-scale tidal effect in the local background, and consistent with Eq. (14) in Schmidt et al. (2018) in the linear regime ($D_+ \lambda_i \ll 1$). It is useful to notice that, after summing the three components of the above equation, i.e. \sum_i , it recovers the isotropic Friedmann equation due to $\sum_i \lambda_i = 0$ in the angle-average sense or for the monopole component of a_{W_i} .

Following the similar concept for the isotropic background case discussed around Eqs. (7) and (9), we introduce the peculiar acceleration along each coordinate axis in the local background as

$$\dot{u}_{W_i} = -\partial_{x_{W_i}} \phi_{\text{tot}} - a_{W_i} \ddot{a}_{W_i} x_{W_i}. \quad (36)$$

A sensible choice for the peculiar potential to absorb the second term is

$$\Phi_W = a \left[\phi_{\text{tot}} + \frac{1}{2} \sum_i a_{W_i} \ddot{a}_{W_i} x_{W_i}^2 \right], \quad (37)$$

This is consistent with the Hamiltonian (see Sec. 2.4) as

$$\dot{u}_{W_i} = -\frac{1}{a} \frac{\partial \Phi_W}{\partial x_{W_i}}. \quad (38)$$

Since the peculiar gravitational potential defined above arises from the *inhomogeneous* matter distribution, $\nabla_{\mathbf{x}}^2 \Phi_W = 4\pi G \bar{\rho}_0 \delta(\mathbf{x}, t)$. Our tasks are to express the peculiar gravitational potential in terms of variables in the local background with anisotropic expansion, a_{W_i} . From Eq. (33), the Poisson equation for the peculiar gravitational potential is expressed as

$$\sum_i \left(\frac{1}{a_{W_i}} \frac{\partial}{\partial x_{W_i}} \right)^2 \Phi_W = \frac{4\pi G \bar{\rho}_0 \delta}{a_{W_1} a_{W_2} a_{W_3}}. \quad (39)$$

We rewrite this in Fourier space for the PM force calculation as

$$\begin{aligned} \ddot{\Phi}_{W, \mathbf{k}_W} &= -\frac{4\pi G \bar{\rho}_0 \tilde{\delta}_{\mathbf{k}_W}}{a_{W_1} a_{W_2} a_{W_3} \sum_i (k_{W_i}/a_{W_i})^2} \\ &= -\frac{4\pi G \bar{\rho}_0 \tilde{\delta}_{\mathbf{k}_W}}{a_{W_1} a_{W_2} a_{W_3}} G_W(k_W), \end{aligned} \quad (40)$$

where $\sum_i (k_{Wi}/\alpha_{Wi})^2 = \sum_i k_i^2 = k^2$ is the square of global isotropic comoving wavenumber reexpressed in terms of that in the anisotropic ‘‘simulation’’ coordinates, and $G_W(k_W) \equiv 1/[\sum_i (k_{Wi}/\alpha_i)^2]$ is the Green function, which is also kept unchanged when it is expressed by the wavenumber in the global comoving coordinate, $G_W(k_W) \rightarrow G(k) = 1/k^2$. This suggests that we need to modify the Green function in the local comoving coordinate, i.e. the SU simulation coordinate. We do not have to change the density assignment for the PM force calculation. Thus we keep the grid for the density assignment to be equally spaced in the local comoving coordinate. We also need to express the split function between the PM and the Tree forces in terms of the local comoving coordinate variables. We use the function which splits isotropically in the global comoving coordinate:

$$\exp \left[- \sum_i (k_{Wi}/\alpha_{Wi})^2 x_s^2 \right]. \quad (41)$$

Again, because of $\sum_i (k_{Wi}/\alpha_{Wi})^2 = k^2$, this recovers the split function in the global comoving coordinate. x_s is a constant, and we set $x_s = 4.5L_{\text{box}}/N_{\text{grid}}^{1/3}$ in the SU simulation.

2.3 Tree force in an anisotropic SU simulation

In the anisotropic case, the Tree acceleration is

$$\begin{aligned} - \frac{\partial \Phi_W^T}{\partial x_{Wi}} \Big|_{\mathbf{x}_{Wn}} &= -Gm\alpha_{Wi} \sum_{n', n' \neq n} \frac{x_{n,i} - x_{n',i}}{|\mathbf{x}_n - \mathbf{x}_{n'}|^3} \\ &\times \left[\operatorname{erfc} \left(\frac{|\mathbf{x}_n - \mathbf{x}_{n'}|}{2x_s} \right) + \frac{|\mathbf{x}_n - \mathbf{x}_{n'}|}{x_s \sqrt{\pi}} \exp \left(- \frac{|\mathbf{x}_n - \mathbf{x}_{n'}|^2}{4x_s^2} \right) \right]. \end{aligned} \quad (42)$$

Note that variables on the r.h.s. must be rewritten in terms of variables in the local comoving coordinate in the actual code implementation, e.g. $x_{n,i} = \alpha_{Wi} x_{Wn,i}$ and $|\mathbf{x}_n - \mathbf{x}_{n'}| = [\sum_i \{(\alpha_{Wi})^2 (x_{Wn,i} - x_{Wn',i})^2\}]^{1/2}$. In the case of Eq. (42), the Tree force is cut isotropically in the global comoving coordinate consistently to the PM force. Comparing to Eq. (14), we need to multiply an additional factor of α_{Wi} to take account the difference between \mathbf{x} and \mathbf{x}_W in the derivative. We use the softening kernel form same as the standard isotropic case. Thus the final form of the Tree acceleration in the anisotropic case is

$$\begin{aligned} - \frac{\partial \Phi^T}{\partial x_{Wi}} \Big|_{\mathbf{x}_{Wn}} &= G\alpha_{Wi} \sum_{\text{group}} M_{\text{group}} g_1(y_{\text{group}}) y_{\text{group},i} \\ &\times \left[\operatorname{erfc} \left(\frac{y_{\text{group}}}{2x_s} \right) + \frac{y_{\text{group}}}{x_s \sqrt{\pi}} \exp \left(- \frac{y_{\text{group}}^2}{4x_s^2} \right) \right], \end{aligned} \quad (43)$$

where $y_{\text{group}} = [\sum_i \{(\alpha_{Wi})^2 (x_{Wn,i} - x_{W\text{group},i})^2\}]^{1/2}$ and so on.

2.4 The drift and kick factors from the anisotropic Hamiltonian

We consider the Hamiltonian for a system of N -body particles in the local background with anisotropic expansion. The physical velocity of the n -th particle in the local background

is given as

$$\frac{d(\alpha_{Wi} x_{Wn,i})}{dt} \simeq \alpha_{Wi} \left(a \frac{dx_{Wn,i}}{dt} + x_{Wn,i} \frac{da}{dt} \right), \quad (44)$$

where we have assumed that α_i is nearly constant during an infinitesimal time interval (see Schmidt et al. 2018). The first term is the peculiar velocity and the second one is the Hubble flow in the local coordinate. The canonical momentum is

$$p_{Wn,i} = m a_{Wi}^2 \dot{x}_{Wn,i}. \quad (45)$$

The kinetic term of the Hamiltonian $H_{W\text{kin}}$ is

$$H_{W\text{kin}} = \sum_n \sum_i \frac{p_{Wn,i}^2}{2m a_{Wi}^2}. \quad (46)$$

The potential term is

$$H_{W\text{pot}} = \frac{1}{2} \sum_n \frac{m \Phi_W(\mathbf{x}_{Wn})}{a}. \quad (47)$$

The total Hamiltonian in the local background that describes the gravitational system for the spatially-inhomogeneous matter distribution is

$$H_W = \sum_n \sum_i \frac{p_{Wn,i}^2}{2m a_{Wi}^2} + \frac{1}{2} \sum_n \frac{m \Phi_W(\mathbf{x}_{Wn})}{a}. \quad (48)$$

The resulting canonical equations of motion are

$$\dot{x}_{Wn,i} = \frac{\partial H_W}{\partial p_{Wn,i}} = \frac{1}{a_{Wi}^2} \frac{p_{Wn,i}}{m}, \quad (49)$$

$$\dot{p}_{Wn,i} = - \frac{\partial H_W}{\partial x_{Wn,i}} = - \frac{m}{a} \frac{\partial \Phi_W(\mathbf{x}_{Wn})}{\partial x_{Wn,i}} \quad (50)$$

As we do in the isotropic case, we obtain the drift and kick factors employed as the time-evolution operators in GADGET-2 for the SU simulation case:

$$I_{\text{drift}, i} = \int_t^{t+\Delta t} \frac{dt}{a_{Wi}^2} \simeq \frac{1}{a_{Wi}^2} \int_t^{t+\Delta t} \frac{dt}{a^2}, \quad (51)$$

$$I_{\text{kick}} = \int_t^{t+\Delta t} \frac{dt}{a}, \quad (52)$$

i.e., the drift factor becomes anisotropic and the kick factor remains isotropic in the local coordinate (SU simulation coordinate). We assumed α_{Wi} to be constant during a time step adopted in the simulation.

2.5 Summary: SU simulation implementation

In summary we made the following changes in the GADGET-2 code to implement the SU simulation including the effect of super-box tidal force into the local background with anisotropic expansion.

- solve the effective Friedmann equation (Eq. 35) to obtain the scale factor in the local background, $a_{Wi}(t)$, along each coordinate axis that describes an anisotropic expansion. In this paper we use the publicly available code given in Schmidt et al. (2018) to obtain $a_{Wi}(t)$ that is accurate up to $O(K^2)$. If $|K_i| = D_+ |\lambda_i| \ll 1$ holds during epochs of a simulation, we can find that $a_{Wi}(t) = a(t) \alpha_{Wi}(t) \simeq a(t)(1 - D_+ \lambda_i)$ is a solution, for the growth rate $D_+(t)$ in the global background cosmology and for the input tidal tensor, λ_i .

• the PM part of the peculiar gravitational force that is sourced by the matter density fluctuation field (spatially-inhomogeneous source):

- the Green function: $1/[\sum_i k_i^2] \rightarrow 1/[\sum_i (k_{Wi}/\alpha_{Wi})^2]$
- the cosmic mean density: $\bar{\rho}_0 \rightarrow \bar{\rho}_0/(\alpha_1\alpha_2\alpha_3)$
- the split factor: $\exp(-\mathbf{k}^2 x_s^2) \rightarrow \exp[-\sum_i (k_{Wi}/\alpha_{Wi})^2 x_s^2]$

• the Tree part:

- multiply an additional factor α_{Wi} to the acceleration
- the positions and the distances: e.g., $x_{n,i} \rightarrow \alpha_{Wi} x_{Wn,i}$, $|\mathbf{x}_n - \mathbf{x}_{n'}| \rightarrow [\sum_i \{(\alpha_{Wi})^2 (x_{Wn,i} - x_{Wn',i})^2\}]^{1/2}$

- the drift factor: $\int_t^{t+\Delta t} a^{-2} dt \rightarrow \alpha_{Wi}^{-2} \int_t^{t+\Delta t} a^{-2} dt$

Our implementation of SU simulations differs from that in Schmidt et al. (2018) for details of the numerical methods, and therefore our method gives another consistency test of SU simulations. In particular, the kick factor in Schmidt et al. (2018) is anisotropic as $\alpha_{Wi}^{-1} \int_t^{t+\Delta t} a^{-1} dt$.

3 THE RESPONSE FUNCTION OF MATTER POWER SPECTRUM TO THE LARGE-SCALE TIDAL FORCE

In this paper we use the SU simulations including the large-scale tidal effect to calibrate the “response” function of the matter power spectrum, which describes how the matter power spectrum of sub-box modes responds to the large-scale tidal force (Dai et al. 2015; Ip & Schmidt 2017; Akitsu et al. 2017; Schmidt et al. 2018; Akitsu et al. 2019).

3.1 Growth and dilation responses

For a finite volume survey, we can sample only sub-survey modes of the fluctuations, and can measure the statistics, here mainly focused on the matter power spectrum, measured from the local volume. The super-survey tidal force, which is not a direct observable, affects the matter power spectrum in the local volume through the mode coupling in nonlinear structure formation. As a result, the band power measured from the local volume is modulated depending on the degree of alignments between \mathbf{k} and the large-scale tidal tensor (Akitsu et al. 2017). That is, the power spectrum acquires a dependence on the direction of \mathbf{k} , in addition to the length $|\mathbf{k}|$: $P(\mathbf{k}; K)$ in the presence of the super-survey tidal effect, K_{ij} . Using the Taylor expansion we can express $P(\mathbf{k}; K)$ to the first-order of K_{ij} as

$$\begin{aligned} P(\mathbf{k}; K) &\simeq P(\mathbf{k}; K=0) + \left. \frac{dP(\mathbf{k}; K)}{dK_{ij}} \right|_{K=0} K_{ij} \\ &= P(k) [1 + R_K(k) \hat{k}_i \hat{k}_j K_{ij}], \end{aligned} \quad (53)$$

where $P(\mathbf{k}; K_{ij} = 0)$ is the power spectrum for the global background in the absence of the super-survey tidal effect, which therefore depends only on the length of wavenumber, i.e. $P(\mathbf{k}; K_{ij} = 0) = P(k)$. Here we introduced the so-called *response function*, $R_K(k; t)$, that describes a response of the

matter power spectrum to the super-survey tidal tensor, defined as

$$R_K(k; t) \hat{k}_i \hat{k}_j \equiv \left. \frac{1}{P(k)} \frac{dP(\mathbf{k}; K)}{dK_{ij}} \right|_{K=0}, \quad (54)$$

and $\hat{\mathbf{k}}$ is the normalized k vector as $\hat{k}_i = k_i/\sqrt{\sum_i k_i^2}$. The second term in Eq. (53) describes a modulation in the power spectrum measured from a local volume under the super-survey tidal tensor K_{ij} .

The SU simulation is equivalent to the case that structure formation is simulated in the global background with a sufficiently large volume, including long-wavelength perturbations, and then the power spectrum is measured from a sub-volume of the large-scale simulation box, corresponding to the volume of SU simulation. Since we do not consider the super-survey density contrast, i.e. $\delta_b = 0$, we have $\bar{\rho}_W = \bar{\rho}$ at the first order of K_{ij} and the Hubble constant in the local volume is not modified, $h_W = h$, unlike the case for δ_b in Li et al. (2014a). Hence, even if the power spectrum has a dimension of $[(h^{-1}\text{Mpc})^3]$, the relation $P(\mathbf{k}, K) = P_W(\mathbf{k}_W, K)$ holds, where $k_{Wi} = k_j(\delta_{ij}^K - K_{ij})$ and P_W is the same power spectrum in the local volume but it takes the wavevector in the local comoving coordinate in the first argument. Following the method in Li et al. (2014a) (see around Eq. 47 in their paper), we can use the chain rule to compute the derivative in Eq. (54) to the first order of K_{ij} as

$$\begin{aligned} &\left. \frac{dP(\mathbf{k}, K)}{dK_{ij}} \right|_{\mathbf{k}, K=0} \\ &= \left. \frac{\partial P_W(\mathbf{k}_W, K)}{\partial K_{ij}} \right|_{\mathbf{k}_W, K=0} + \frac{\partial P_W(\mathbf{k}_W, K=0)}{\partial k_{Wm}} \frac{\partial k_{Wm}}{\partial K_{ij}} \\ &\simeq \left. \frac{\partial P_W(\mathbf{k}_W, K)}{\partial K_{ij}} \right|_{\mathbf{k}_W, K=0} + \frac{\partial P(k)}{\partial k} \frac{\partial k}{\partial k_m} \frac{\partial k_{Wm}}{\partial K_{ij}} \\ &= \left. \frac{\partial P_W(\mathbf{k}_W, K)}{\partial K_{ij}} \right|_{\mathbf{k}_W, K=0} - \frac{\partial P(k)}{\partial \ln k} \hat{k}_i \hat{k}_j. \end{aligned} \quad (55)$$

The first term on the r.h.s. of the above equation is the “growth” response that describes how the growth of the density perturbation, $\delta_{\mathbf{k}}$, is affected by the large-scale tidal force. The second term denotes the “dilation” response; the modulation in the power spectrum arises from the fact that the comoving wavenumber in the local volume is modulated by the large-scale tidal force via $k_{Wi} = k_j(\delta_{ij}^K - K_{ij})$. Thus we define the growth response as

$$G_K(k) \hat{k}_i \hat{k}_j \equiv \left. \frac{1}{P(k)} \frac{\partial P_W(\mathbf{k}_W, K)}{\partial K_{ij}} \right|_{\mathbf{k}_W, K=0}. \quad (56)$$

Then R_K and G_K are related as

$$R_K(k) = G_K(k) - \frac{\partial \ln P(k)}{\partial \ln k}. \quad (57)$$

Thus the SU simulation gives a useful way to calibrate the growth response. We can consider the dilation response separately from the derivative of the nonlinear power spectrum. The perturbation theory prediction $G_K = 8/7$ (Akitsu et al. 2017; Barreira & Schmidt 2017) can be used to test our anisotropic simulation code at small k in the linear regime.

To compute the growth response, we will measure the following power spectrum measured in the SU simulation

(see around Eq. 25 in Takahashi et al. 2019):

$$\hat{P}_W(k_{W,\text{bin}}, K) = \frac{1}{N(k_{W,\text{bin}})} \sum_{\mathbf{k}_W \in k_{W,\text{bin}}} |\delta_{\mathbf{k}_W}|^2. \quad (58)$$

Here the power spectrum is estimated from the average of $|\delta_{\mathbf{k}_W}|^2$ over a bin given by a spherical shell at radius around $k_{W,\text{bin}}$ with a finite width. Recalling the relation between the wavevectors in the global and local backgrounds, $k_{Wi} = k_i(1 - D_+\lambda_i) = \alpha_{Wi}k_i$, the power spectrum estimated in the above is equivalent to the power spectrum estimated from the average of $|\delta_{\mathbf{k}}|^2$ over the ellipsoidal shell of \mathbf{k} satisfying $k_W^2 = \sum_i (\alpha_{Wi})^2 k_i^2$ when it is seen in the global comoving coordinate. Hence the above estimator gives an estimate of \mathbf{k} -direction dependent power spectrum which we want for the response calibration: $P(\mathbf{k}, K)$. $N(k_W)$ is the number of Fourier modes taken in the summation, which is given by $N(k_{W,\text{bin}}) \simeq 2\pi k_{W,\text{bin}}^2 \Delta k_W V / (2\pi)^3$ at $k_{W,\text{bin}} \gg 2\pi/L$, where Δk_W is the bin width and V is the volume of SU simulation box.

3.2 A calibration method of the growth response

We follow Schmidt et al. (2018) to measure the growth response G_K from the power spectra measured from the SU simulations (Eq. 58). To do so, we employ the three simulations labeled A, B and C. They share the same random-number seed for the generation of the initial conditions, but different λ values: $\lambda_A = \lambda_{A,z}(-0.5, -0.5, 1)$, $\lambda_B = \lambda_{B,z}(-0.5, -0.5, 1) = \lambda_{A,z}(0.5, 0.5, -1) = -\lambda_A$ and $\lambda_C = (0, 0, 0)$. Thus the A and B runs are the anisotropic case and $\delta_b = 0$ due to $\sum_i \lambda_i = 0$, and the C run is the standard isotropic case.

The estimator of G_K is

$$G_K(k) = \frac{\langle [P_{WA}(\mathbf{k}_{WA})\mathcal{L}_2(\hat{k}_{WA,z}) - P_{WB}(\mathbf{k}_{WB})\mathcal{L}_2(\hat{k}_{WB,z})] \rangle}{\langle P_{WC}(\mathbf{k}_{WC})\mathcal{L}_2^2(\hat{k}_z)D_+(t)(\lambda_{A,z} - \lambda_{B,z}) \rangle}, \quad (59)$$

where $\langle \dots \rangle$ is angle averaging, \mathcal{L}_2 is the second-order Legendre polynomial. $P_{WA}(\mathbf{k}_{WA})$, $P_{WB}(\mathbf{k}_{WB})$ and $P_{WC}(\mathbf{k}_{WC})$ are the three dimensional matter power spectrum measured in each simulation frame for the runs of A, B and C, respectively. Note that each simulation and measured G_K can be characterized by a single parameter λ_z and $\lambda_{A,z}$, respectively. Throughout the paper, we frequently use these parameters to present results.

4 SU SIMULATIONS

Here we describe a numerical implementation of SU simulations. We first describe how to generate the initial conditions, and then present the specifications of our simulations. We also study the resolution effects on measurements of the power spectrum from SU simulations.

4.1 Generating initial conditions

To generate the initial conditions, we use the second-order Lagrangian perturbation theory (2LPT; Scoccimarro 1998; Crocce et al. 2006; Nishimichi et al. 2009) and the linear matter power spectrum computed using CAMB (Lewis et al.

2000). Recalling the fact that the growth tidal response function G_K is 8/7 at a sufficiently high redshift or at the leading order of the perturbation theory prediction (Akitsu et al. 2017; Barreira & Schmidt 2017), we change the input linear matter power spectrum, for an assumed large-scale tidal tensor $K_{ij} = D_+(a_{\text{ini}})\lambda_i$ at the initial redshift, as

$$P(\mathbf{k}, a_{\text{ini}}) \rightarrow P_W(\mathbf{k}_W, a_{\text{ini}}) = P(k, a_{\text{ini}}) \left[1 + \frac{8}{7} \hat{k}_i \hat{k}_j K_{ij}(a_{\text{ini}}) \right]. \quad (60)$$

We use this modified matter power spectrum to calculate the initial displacement of particles.

To set up the initial conditions, we also need the initial peculiar velocity field. Rather than analytically deriving the peculiar velocity field in the SU simulation setups, we numerically evaluate it as follows. Recall that the peculiar velocity field for an N -body particle in the local coordinate is given as

$$\frac{d(a_{Wi}x_{Wi})}{dt} \simeq \alpha_{Wi} \frac{d(ax_{Wi})}{dt} = \alpha_{Wi} H \left(x_{Wi} + \frac{dx_{Wi}}{d \ln a} \right), \quad (61)$$

where we ignored a temporal variation of the normalized scale factor $\alpha_{Wi}(t)$ during the time step in a simulation. Hence following the normalization convention of the input and output data for GADGET-2, we calculate the peculiar velocity

$$\sqrt{a_{Wi}} H \frac{dx_{Wi}}{d \ln a}. \quad (62)$$

We first prepare the initial displacement fields at two epochs, $a_{\text{ini}+}$ and $a_{\text{ini}-}$, slightly shifted from the initial redshift on both positive and negative sides, using the same initial seed of the fluctuations from the initial power spectrum (Eq. 60). Then we compute the initial peculiar velocity field for each particle from the numerical differentiation as

$$\sqrt{a_{Wi}(a_{\text{ini}})} H(a_{\text{ini}}) \frac{x_{Wi}(a_{\text{ini}+}) - x_{Wi}(a_{\text{ini}-})}{\ln a_{\text{ini}+} - \ln a_{\text{ini}-}}. \quad (63)$$

In this paper we adopt $d \ln a = \ln a_{\text{ini}+} - \ln a_{\text{ini}-} = 0.02$ for all the simulations. We have tested the accuracy of this step size in the finite differencing by applying it to the isotropic case where the velocities can directly be computed by 2LPT, finding that the errors are less than 5% for more than 97% of particles in our fiducial high resolution runs (see Sec. 4.2).

4.2 SU simulation specifications

Table 1 summarizes our simulation specifications, where N_{part} is the number of particles, z_{ini} is the initial redshift and $(\lambda_x, \lambda_y, \lambda_z)$ are the amplitudes of the tidal tensor normalized to their values today, respectively. For a validation on our choice of the initial redshift z_{ini} , we would like to refer readers to Nishimichi et al. (2019). As we stated, we set the values of λ_x , λ_y and λ_z such that $\lambda_x + \lambda_y + \lambda_z = 0$ and $\lambda_x = \lambda_y = -\lambda_z/2$ for the anisotropic cases, and $\lambda_x = \lambda_y = \lambda_z = 0$ for the isotropic cases. Each simulation set has 16 realizations, and each pair of SU-A/B simulations and the corresponding (C) isotropic simulation share the identical set of 16 random seeds to generate the initial conditions to minimize the effect of sample variance in the response calibration. For each run, we adopt a flat Λ CDM cosmology with $\Omega_{m0} = 0.3156$, $\Omega_{\Lambda} = 0.6844$, $H_0 = 100h = 67.27 \text{ km s}^{-1} \text{ Mpc}^{-1}$, $n_s = 0.9645$ and

Table 1. Summary of our simulation specifications, where N_{part} , z_{ini} and $(\lambda_x, \lambda_y, \lambda_z)$ denote the number of particles, the initial redshift and the amplitudes of the super-box tidal tensor at present, respectively.

Set	N_{part}	z_{ini}	$(\lambda_x, \lambda_y, \lambda_z)$	Realizations
HR1-A	512^3	127	(-0.05, -0.05, 0.1)	16
HR1-B	512^3	127	(0.05, 0.05, -0.1)	16
HR2-A	512^3	127	(-0.005, -0.005, 0.01)	16
HR2-B	512^3	127	(0.005, 0.005, -0.01)	16
HR3-A	512^3	127	(-0.0005, -0.0005, 0.001)	16
HR3-B	512^3	127	(0.0005, 0.0005, -0.001)	16
HR-C	512^3	127	(0, 0, 0)	16
MR-A	256^3	63	(-0.005, -0.005, 0.01)	16
MR-B	256^3	63	(0.005, 0.005, -0.01)	16
MR-C	256^3	63	(0, 0, 0)	16
LR-A	128^3	31	(-0.005, -0.005, 0.01)	16
LR-B	128^3	31	(0.005, 0.005, -0.01)	16
LR-C	128^3	31	(0, 0, 0)	16

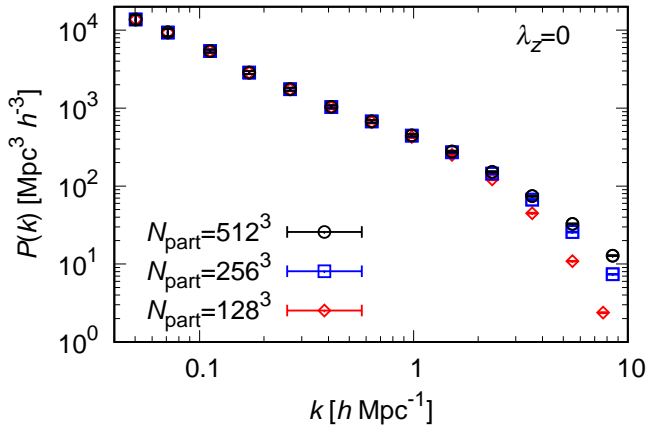


Figure 2. The matter power spectra at $z = 0$ measured from the simulation sets with $N_{\text{part}} = 512^3$ (HR-C), 256^3 (MR-C), 128^3 (LR-C) in the isotropic cases with $\lambda_z = 0$. Comparing the three results manifests the validation range of scales up to which the simulation with respective N_{part} is reliable. The error bars at each k bin denote the error on the mean, estimated from 16 realizations.

$A_s = 2.2065 \times 10^{-9}$ for the global background (Planck Collaboration et al. 2016). We carry out all the simulations using the TreePM mode of the modified GADGET-2 for the local comoving simulation box size of $L_{\text{box}} = 125 h^{-1}$ Mpc on a side, which is sufficiently large so that the super-survey tidal force is safely considered to be in the linear regime. We set the gravitational softening parameter to be $\epsilon = 0.05 \times L_{\text{box}}/N_{\text{part}}^{1/3} = 12.2, 24.4$ and $48.8 h^{-1}$ kpc for the sets with $N_{\text{part}} = 512^3$ (HR), 256^3 (MR) and 128^3 (LR), respectively. We employ N_{grid} Fourier grids for the PM force calculation, and set this parameter to be $2^3 \times N_{\text{part}}$ (i.e., two grids per particle spacing in one dimension).

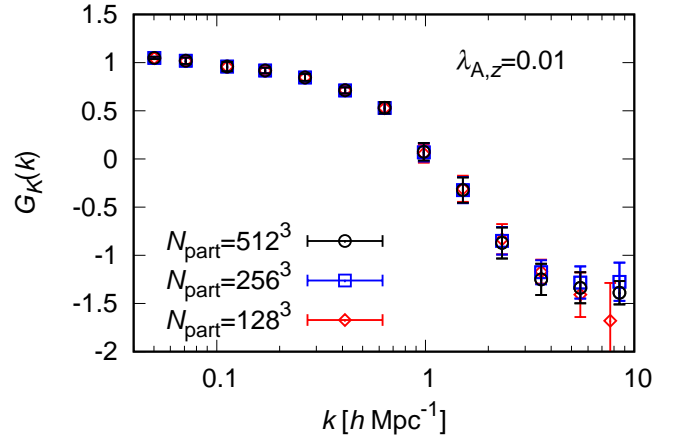


Figure 3. The growth response, $G_K(k)$, at $z = 0$, measured from SU simulations with $\lambda_z = \pm 0.01$ and $N_{\text{part}} = 512^3$ (HR2), 256^3 (MR), 128^3 (LR). We used the estimator (Eq. 59) to evaluate G_K from each paired SU simulations (see Table 1).

4.3 Resolution study

In this subsection we address the validation range of scales where simulation results are considered well converged and reliable. Figure 2 shows the matter power spectra at $z = 0$ measured from the sets of HR-C, MR-C and LR-C, i.e., the isotropic cases with $N_{\text{part}} = 512^3, 256^3$ and 128^3 , respectively. Throughout this paper we show the error bars to denote errors on the mean that are estimated from the standard deviation of 16 realizations divided by $\sqrt{16}$. The figure shows that the simulations of different resolutions start to deviate from each other on scales greater than a certain k , due to the resolution limitation. The LR-C (MR-C) set agrees with the HR-C within 10% up to $k \approx 1.5$ (3) $h \text{ Mpc}^{-1}$. Considering the size of the softening length, we conclude that the HR sets are likely reliable up to $k \approx 6 h \text{ Mpc}^{-1}$.

Figure 3 shows the growth-only tidal response function G_K at $z = 0$ for the three resolutions. For $N_{\text{part}} = 512^3$, we use a combination of the sets of HR2-A, HR2-B and HR-C to measure G_K using the estimator Eq.(59). Similarly, the case of $N_{\text{part}} = 256^3$ (128^3) uses the MR-A, MR-B and MR-C (LR-A, LR-B and LR-C) sets. The λ values are common among the three resolutions as $(\lambda_x, \lambda_y, \lambda_z) = (\mp 0.005, \mp 0.005, \pm 0.01)$ and $(0, 0, 0)$. This setting can be characterized by a single parameter $\lambda_{A,z} = 0.01$. The response function G_K measured from the three resolutions agree with each other within the error bars over the whole range of scales we plot here. This implies that the impact of the limited resolution on the three dimensional power spectrum is very similar for the isotropic and anisotropic cases, and this partially cancels in the estimator of the response function. However, recalling Figure 2, we use the HR sets ($N_{\text{part}} = 512^3$) as our fiducial choice to study the results up to $k \approx 6 h \text{ Mpc}^{-1}$ to be on the safe side.

4.4 The impact of the periodic boundary conditions

In this section we study the impact of the periodic boundary condition, i.e. a possible artifact due to the choice of

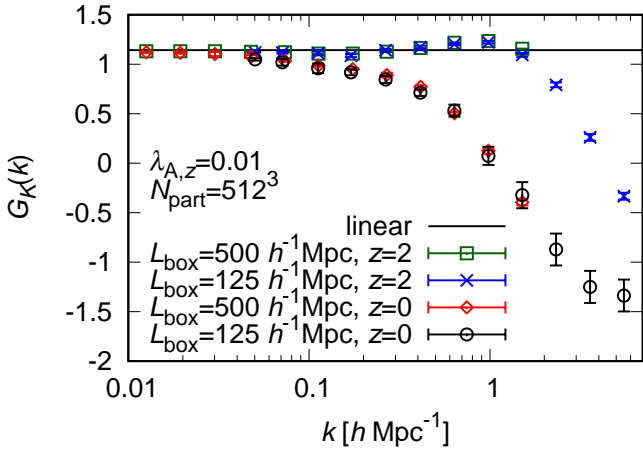


Figure 4. The growth response functions $G_K(k)$ at $z = 0, 2$ from the SU simulations with $L_{\text{box}} = 125, 500 h^{-1}\text{Mpc}$, $N_{\text{part}} = 512^3$ and $\lambda_{A,z} = 0.01$. The solid line shows the perturbation theory prediction of $G_K = 8/7$.

the simulation box size. Our anisotropic SU simulations incorporate the effect of the super-box tidal force with wavelengths *much longer* than a box size L_{box} . This is equivalent to an approximation to ignore all the higher-order terms in the long-wavelength gravitational potential; that is, we ignore the contributions of $O(\nabla^n \Psi^L|_{\mathbf{x}_0} (\Delta x)^n)$ with $n \geq 3$, in Eq. (19). If we cut out a finite-volume sub-box realization from a large-box simulation, the super-box tidal force for the realization should include contributions from all the Fourier modes, around the box, including the modes comparable with the sub-box size that correspond to the higher-order terms we ignore. Such intermediate-wavelength modes are incompatible with the periodic boundary conditions employed in a SU simulation. To study the limitation of the approximation, ideally, we can extend the method for super-survey density contrast (δ_b) in Fig. 2 of Li et al. (2014b) to the super-survey tidal force to test how the SU approach can accurately simulate the structure formation, even in the average sense. However, this is beyond the scope of this paper. Instead we use a larger-size box simulation to study how the results are sensitive to a chosen size of simulation box.

Figure 4 compares the growth tidal response G_K at $z = 0$ and 2 from the simulations with different box sizes of $L_{\text{box}} = 125$ and $500 h^{-1}\text{Mpc}$ (we will discuss in more detail the results of the growth response in the next section, so here let us focus on the comparison). The $L_{\text{box}} = 500 h^{-1}\text{Mpc}$ run employs $N_{\text{part}} = 512^3$ and $\lambda_{A,z} = 0.01$ in four realizations, and includes Fourier modes whose wavelengths are longer than the box size of another simulation, $L = 125 h^{-1}\text{Mpc}$. The mass and spatial resolutions of the $L_{\text{box}} = 500 h^{-1}\text{Mpc}$ run are as same as the LR sets. According to the resolution study discussed in Sec. 4.3, the results from the $L_{\text{box}} = 500 h^{-1}\text{Mpc}$ should be reliable up to $k = 1.5 h \text{Mpc}^{-1}$. We confirm that the results for the different box sizes are consistent with each other in the reliable range of k . Thus we conclude that $L_{\text{box}} = 125 h^{-1}\text{Mpc}$ is large enough to measure the tidal response at $z \leq 2$. A larger-box simulation allows us to explore G_K at smaller- k . We find that G_K from the $L_{\text{box}} = 500 h^{-1}\text{Mpc}$ run well agrees with the perturbation

theory prediction even at $k \geq 0.01 h \text{Mpc}^{-1}$. Thus as long as a simulation box size is in the linear regime at an output redshift, we can use SU simulations of arbitrary box size to estimate the response function. This is the similar condition to that for a SU simulation of the super-survey density contrast (δ_b) (Li et al. 2014a).

Hence hereafter we use the simulations of box size $L_{\text{box}} = 125 h^{-1}\text{Mpc}$ as our default choice.

5 RESULTS

In this section we show the main results of this paper, i.e. the SU simulation results for the growth response function for the large-scale tidal force. In particular we present a validation of the response function computed from the TreePM code in the linear and nonlinear regimes by comparing the results with the perturbation theory results at large scales (small k) and with those from higher-resolution PM simulations.

5.1 Monopole power spectrum: a sanity check of anisotropic SU simulations

Before going to the main results, we study the monopole power spectrum measured from the SU simulations. Although the large-scale tidal force causes an anisotropic distortion in the matter power spectrum depending on the alignments between the wavevector \mathbf{k} and the tidal tensor K_{ij} , the monopole spectrum should not be changed due to the traceless nature (Akitsu et al. 2017). Hence, the monopole spectrum measured from SU simulations should be free of the large-scale tidal effect to within the measurement errors, if SU simulations are properly implemented. Hence this gives a useful sanity check of SU simulations.

First we analytically check that the monopole spectrum measured in SU simulations should be free of the large-scale tidal effect. The monopole power spectrum is computed as

$$\begin{aligned}
 \langle P_W(\mathbf{k}_W, K) \rangle &= \frac{1}{4\pi} \int P_W(\mathbf{k}_W, K) \sin \theta_{\mathbf{k}_W} d\theta_{\mathbf{k}_W} d\phi_{\mathbf{k}_W} \\
 &\simeq \frac{1}{4\pi} \int P(k) [1 + G_K(k) \hat{k}_i \hat{k}_j K_{ij}] \sin \theta_{\mathbf{k}_W} d\theta_{\mathbf{k}_W} d\phi_{\mathbf{k}_W} \\
 &= P(k) \left[1 + \frac{G_K(k)}{4\pi} \int \hat{k}_i \hat{k}_j K_{ij} \sin \theta_{\mathbf{k}_W} d\theta_{\mathbf{k}_W} d\phi_{\mathbf{k}_W} \right] = P(k),
 \end{aligned} \tag{64}$$

where $\theta_{\mathbf{k}_W}, \phi_{\mathbf{k}_W}$ are the polar coordinate in the Fourier space and we have used the traceless condition of K_{ij} as

$$\begin{aligned}
 &\frac{1}{4\pi} \int \hat{k}_i \hat{k}_j K_{ij} \sin \theta_{\mathbf{k}_W} d\theta_{\mathbf{k}_W} d\phi_{\mathbf{k}_W} \\
 &= \frac{1}{4\pi} \int \hat{k}_i \hat{k}_j K_i \delta_{ij}^K \sin \theta_{\mathbf{k}_W} d\theta_{\mathbf{k}_W} d\phi_{\mathbf{k}_W} \simeq \frac{k_W^2}{3k^2} \sum_i K_i = 0.
 \end{aligned} \tag{65}$$

Figure 5 clearly shows the monopole power spectra measured from SU simulations with $N_{\text{part}} = 512^3$ and $\lambda_z = 0.1$ (HR1-A), -0.1 (HR1-B) and 0 (HR-C) well agree with each other. To see in more detail, we show fractional differences between the power spectra of the isotropic and anisotropic runs in Figure 6. All results are very close to zero better

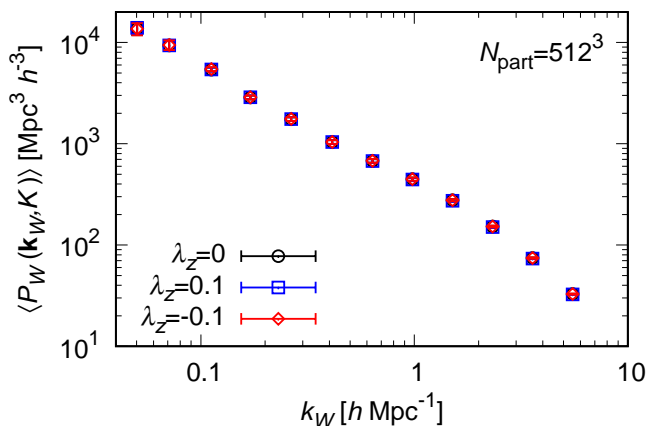


Figure 5. The monopole power spectra at $z = 0$, measured from SU simulations with $N_{\text{part}} = 512^3$ and $\lambda_z = 0.1$ (HR1-A) and -0.1 (HR1-B), respectively. The monopole power spectrum should be free of the large-scale tidal effect if the SU simulations are properly done, as discussed in Section 5.1. These results can be compared with the matter power spectrum measured from the isotropic background simulation (i.e. the standard simulation), with $N_{\text{part}} = 512^3$ and $\lambda_z = 0$ (HR-C).

than a sub percent in the fractional amplitude for the cases of $|\lambda_z| = 0.01$ and 0.001 over the range of k we study. The results for $|\lambda| = 0.1$ shows a percent-level deviation, implying a nonlinear contribution of $O(K^2)$, i.e. a violation of the linear response formula. Therefore the $|\lambda_z|$ values less than 0.01 are safer to obtain the linear response function to K_{ij} , being not affected by the higher-order effect of K_{ij} .

5.2 Growth response $G_K(k)$ in the linear and nonlinear regimes

In Figure 7 we study the growth response, $G_K(k)$, measured from the paired SU simulations with $N_{\text{part}} = 512^3$ and $\lambda_{A,z} = 0.001$ (HR3), 0.01 (HR2) and 0.1 (HR1), using the estimator Eq. (59). All the results for G_K remarkably well agree with each other over the range of scales we consider, to within the statistical error bars. One notable advantage is the use of paired SU simulations using the same initial seeds allow for an accurate calibration of the growth response, $G_K(k)$, even at very small k , where the sample variance is large. Conversely, the results at small scales $k \gtrsim 1 h \text{ Mpc}^{-1}$ appear to be relatively noisy.

Figure 8 shows how the growth response, $G_K(k; z)$, evolves with redshift, measured from the simulation sets of HR2-A, HR2-B and HR-C, i.e., $N_{\text{part}} = 512^3$, $\lambda_{A,z} = 0.01$. The solid line gives the perturbation theory prediction of $G_K = 8/7$ (Akitsu et al. 2017), which should be valid at the limit of $k \rightarrow 0$. By construction of the initial conditions, the simulations at $z = 127$ reproduces $G_K = 8/7$ (see around Eq. 60). As structure evolves, the simulation results start to deviate from the perturbation theory prediction due to the nonlinear mode coupling; the SU simulations lead to the smaller amplitudes in the growth response in the weakly nonlinear regime, and the response eventually turns to be negative at smaller scales (Schmidt et al. 2018). Comparing the results at different redshifts also manifests that the sim-

ulation results match the perturbation theory prediction up to higher k for higher redshifts, as expected. At $z = 0$, the nonlinear effect is important already at $k \gtrsim 0.1 h \text{ Mpc}^{-1}$. We have compared our results at $z = 0, 1$ with Schmidt et al. (2018), and found that the agreements are fairly good.

Figure 9 gives a validation of the TreePM based SU simulation, addressing whether our Tree part computes gravity in the anisotropic SU simulation properly. As we stated above, our PM part works well because G_K in the linear scales agrees with the perturbation theory prediction of $G_K = 8/7$ (see also Figure 4 for the agreement between the results from the larger-box run and the perturbation theory prediction at smaller- k , $k \gtrsim 0.01 h \text{ Mpc}^{-1}$). To test the implementation of the Tree part, we additionally perform two PM-only runs, and compare their results with the TreePM result for G_K . One of the PM-only runs employ $N_{\text{grid}} = 512^3$ as in our default TreePM run. The difference between the two runs is whether the short range force is supplemented by the Tree force or not. Then we use the higher-resolution PM-only run with $N_{\text{grid}} = 2048^3$ to validate the TreePM run, by supplementing the gravitational force on small separations with the refined grid resolution. We run the high-resolution PM runs assuming a set of the three initial conditions as in the sets of HR2-A, HR2-B and HR-C. We find that the PM run with $N_{\text{grid}} = 512^3$ underpredicts the G_K amplitudes by up to 40% at $k > 1 h \text{ Mpc}^{-1}$ compared to the PM run with $N_{\text{grid}} = 2048^3$. On the other hand, the TreePM run with $N_{\text{grid}} = 512^3$ agrees with the high-resolution PM run to within 5% level even at $k > 1 h \text{ Mpc}^{-1}$. This agreement is encouraging because it means that the Tree part in our SU simulation properly solves gravity in structure formation down to small scales. The slight mismatch at the two largest k bins between the TreePM and the PM-only run with the larger number of grids would be a sign that the latter starts to fail to resolve the force. Unlike the adaptive nature of the force resolution from a TreePM calculation, the fixed force resolution with the PM-only runs should eventually see a breakdown. Since the lower resolution PM-only run (with $N_{\text{grid}} = 512^3$) starts to deviate from the other two at around $k \simeq 1 h \text{ Mpc}^{-1}$, the higher-resolution PM-only run, which has four times higher resolution per dimension ($N_{\text{grid}} = 2048^3$), is expected to perform poorly at $k \simeq 4 h \text{ Mpc}^{-1}$. This is indeed about the scale at which the TreePM run and the higher-resolution PM-only run start to deviate. Therefore, we conclude that our TreePM implementation works as expected compared to the PM-only runs.

5.3 Total response $R_K(k)$ in the linear and nonlinear regimes

Finally we study the full response that is given by a sum of the growth response and the dilation response: $R_K \equiv G_K - \partial \ln P(k) / \partial \ln k$ (see Eq. 57). We use the emulator COSMIC EMU (Heitmann et al. 2016; Lawrence et al. 2017) to evaluate the dilation term $\partial \ln P / \partial \ln k$ that should be valid up to the nonlinear scales. The figure clearly shows that the total response has a k -dependence, and has smaller amplitudes at very large k , indicating an asymptotic behavior of $R_K \rightarrow 0$ at very large k . However, up to $k \simeq 6 h \text{ Mpc}^{-1}$, the total response has a non-vanishing value, $R_K > 0$, meaning that the large-scale tidal force affects structure formation even at

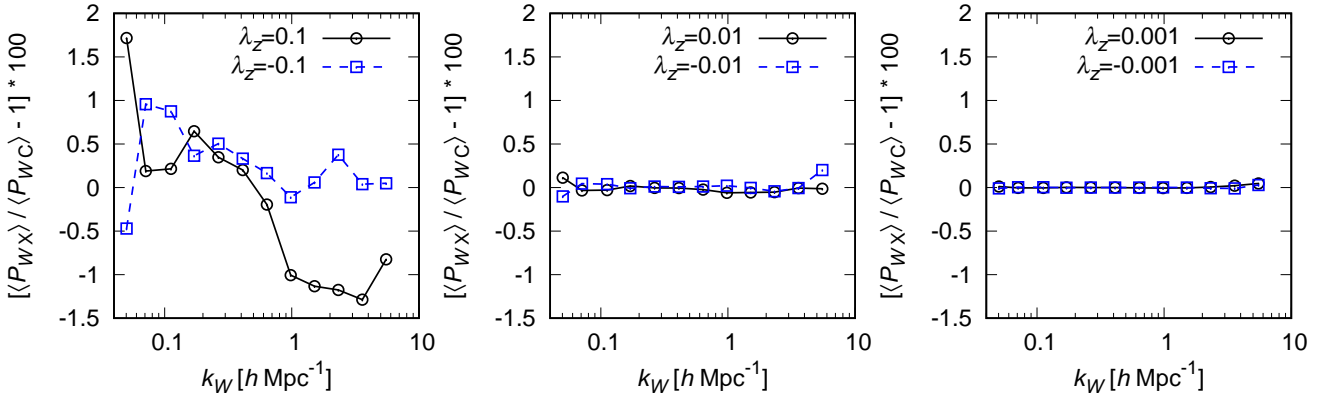


Figure 6. Similar to the previous figure, but each panel shows the fractional difference of the monopole power spectra for the SU simulations relative to the power spectrum in the isotropic universe simulation, denoted as $\langle P_{WC} \rangle$. Here we show the results for the SU simulations with $\lambda_z = \pm 0.1$ (HR1), ± 0.01 (HR2) and ± 0.001 (HR3) from left to right panels, respectively. The subscript “X” in $\langle P_{WX} \rangle$ denotes the SU simulation runs with “A” or “B” in Table 1.

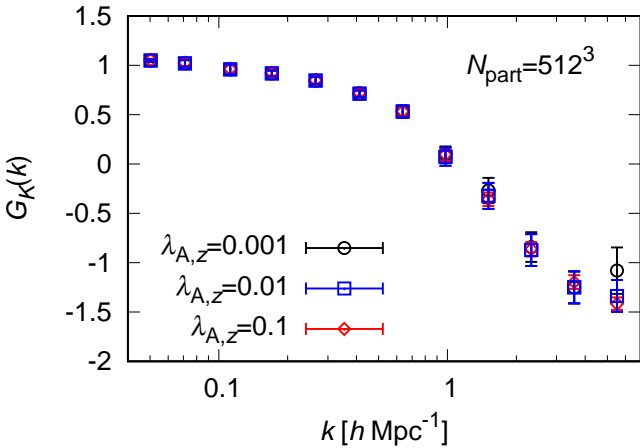


Figure 7. The growth response, $G_K(k)$, at $z = 0$, measured from paired SU simulations with $N_{\text{part}} = 512^3$ and $\lambda_z = \pm 0.001$ (HR3), ± 0.01 (HR2) and ± 0.1 (HR1).

such small scales. Note that the baryonic acoustic oscillation features at $k \approx 0.1 \text{ h Mpc}^{-1}$ are not seen due to our sparse k -binning.

6 CONCLUSION AND PROSPECTS

In this paper we have developed a TreePM cosmological N -body simulation code to simulate structure formation in a finite volume including the effect of super-box tidal force (K_{ij}) on sub-box modes. To do this, we have presented a formulation to include the effect of super-box tidal force into the anisotropic background expansion, which can be done by introducing the anisotropic scale factor, $a_{Wi}(t)$ – so-called anisotropic separate universe (SU) simulation. We modified the public N -body code, GADGET-2, to implement SU simulations for the Λ CDM cosmology. Extending the “isotropic” SU simulation technique for the super-box density contrast δ_b , which has been developed by many groups (Li et al. 2014a; Wagner et al. 2015a; Baldauf et al. 2016), we mod-

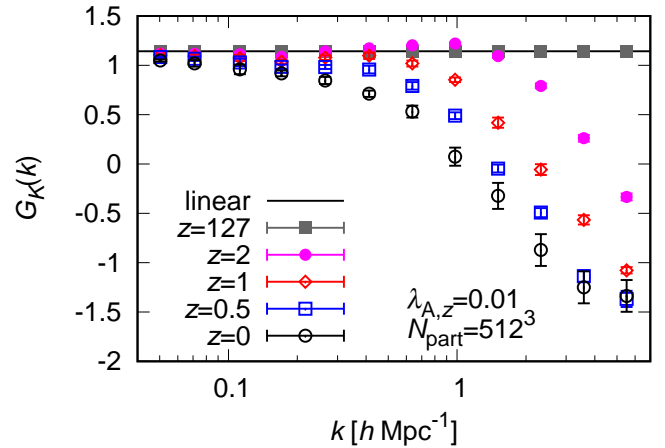


Figure 8. Shown is how the growth response evolves with redshifts; the results measured from the SU simulations at outputs $z = 127, 2, 1, 0.5$ and 0 , respectively, are shown. We used the SU simulations with $N_{\text{part}} = 512^3$ and $\lambda_z = \pm 0.01$ (HR2). The solid line shows the perturbation theory prediction of $G_K = 8/7$ that should hold at the limit of $k \rightarrow 0$.

ified both parts of PM force and Tree force to include the super-box tidal effects on structure formation on both large- and small-scales up to the deeply nonlinear regime. The modification of PM force is straightforward. However, the modifications of Tree force and the split factor that divides the forces into the PM and Tree forces are not trivial, and our treatment is slightly different from the previous work (Schmidt et al. 2018). We have tested and validated our method by comparing the simulation results with the perturbation theory predictions and with the result from high-resolution PM code (Figures 5 – 8 and 9). We also study the impact of the periodic boundary condition on anisotropic SU simulations in Figure 4.

We used the SU simulations to calibrate the “response” function of the matter power spectrum that describes how the super-box tidal force affects the matter power spectrum as a function of wavenumber and redshift, for a given global

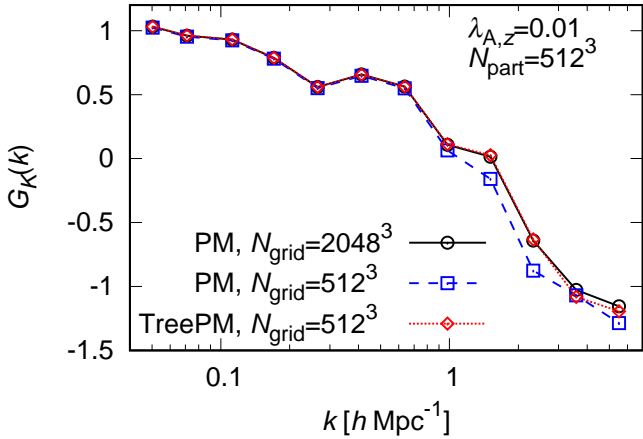


Figure 9. A validation of the growth response measurement using the TreePM run with $N_{\text{grid}} = 512^3$ and $\lambda_z = \pm 0.01$ in our SU simulation implementation, compared with the high-resolution PM-only SU simulation with $N_{\text{grid}} = 2048^3$. For comparison we also show the result for the PM-only simulation with $N_{\text{grid}} = 512^3$.

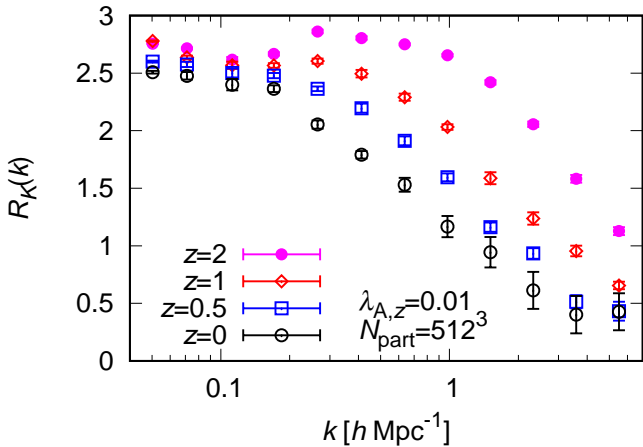


Figure 10. The total response to the large-scale tidal force at different redshifts, which is given by a sum of the growth response and the dilation response: $R_K(k) = G_K(k) - \partial \ln P(k) / \partial \ln k$. We used the SU simulations with $N_{\text{part}} = 512^3$ and $\lambda_z = \pm 0.01$ (HR2) to evaluate the growth response, and employ the emulator COSMIC EMU (Heitmann et al. 2016; Lawrence et al. 2017) to evaluate the dilation response for the nonlinear power spectrum, $\partial \ln P(k) / \partial \ln k$.

cosmological model, the standard adiabatic Λ CDM model considered in this paper. With the aid of the TreePM SU simulations, we studied the response function over a wide range of scales from the linear to deeply nonlinear regimes, $0.05 < k/[h \text{ Mpc}^{-1}] \lesssim 6$. We showed that the response function has a characteristic k -dependence, and the large-scale tidal force affects structure formation over all the scales we have considered, i.e. down to the deeply nonlinear regime (Figures 8 and 10).

As discussed in Li et al. (2014b) (also see Akitsu et al. 2017), the leading-order response of large-scale fields to small-scale structure formation arises from the super-survey

density contrast (δ_b) and the super-survey tidal tensor (K_{ij}) that are both from the second derivative tensor of the long-wavelength gravitational potential, reflecting the nature of the second-derivative differential equations in Newtonian (Einstein) gravity. Hence a combination of isotropic and anisotropic SU simulations allows one to simulate structure formation in a finite volume, with periodic boundary conditions, not only including the effects of both super-box modes, but also keeping high resolution to accurately simulate nonlinear structure formation. As long as the density fluctuations of a simulation box size are in the linear regime, SU simulations are valid. In particular, the use of TreePM code based SU simulations allows one to simulate nonlinear structure formation including the effects of super-box modes on properties of halos where galaxies and galaxy clusters form, which therefore have direct connections to large-scale structure observables.

There are many applications of anisotropic SU simulations to large-scale structure cosmology. Such applications include an accurate calibration of the tidal bias of halos and galaxies (Baldauf et al. 2012; Moradinezhad Dizgah & Dvorkin 2018), the effects on redshift-space clustering of galaxies (Akitsu et al. 2017; Akitsu & Takada 2018; Akitsu et al. 2019), a calibration of the covariance matrix for the redshift-space power spectrum and weak lensing (Akitsu et al. 2017; Li et al. 2018; Barreira et al. 2018; Wadekar & Scoccimarro 2019), the intrinsic alignments of halo/galaxy shapes (Schmidt & Jeong 2012; Schmidt et al. 2015; Chisari et al. 2016; Okumura et al. 2018; Okumura & Taruya 2020; Taruya & Okumura 2020) (also see Kurita, Takada et al. in preparation), cosmology with optical clusters (Osato et al. 2018; Sunayama et al. 2020), the effects on galaxy formation in hydrodynamical simulations (Barreira et al. 2019), the effects on cosmic reionization and physics of intergalactic medium (D’Aloisio et al. 2020), and so on. These are all interesting and worth to explore, and this is a list for our future work.

While this paper is under completion, the preprint (Stücker et al. 2020) was put forward in arXiv. Our work is based on a similar motivation, but independent and is not affected by their work.

ACKNOWLEDGEMENTS

We would like to thank the referee of this paper Vincent Desjacques for useful comments. We would like to appreciate Volker Springel and Andreas S. Schmidt for making their codes publicly available. We would like to thank Kazuyuki Akitsu and Yin Li for useful discussion. We would like to acknowledge Yosuke Kobayashi for providing us with an analysis code of simulation data. All simulations were carried out on Cray XC50 at Center for Computational Astrophysics, National Astronomical Observatory of Japan. This work was supported in part by World Premier International Research Center Initiative (WPI Initiative), MEXT, Japan, JSPS KAKENHI Grant Numbers JP15H03654, JP15H05887, JP15H05893, JP15H05896, JP15K21733, JP17K14273 and JP19H00677, and Japan Science and Technology Agency CREST JPMHCR1414.

REFERENCES

- Aihara H., et al., 2018, *PASJ*, **70**, S4
- Akitsu K., Takada M., 2018, *Phys. Rev. D*, **97**, 063527
- Akitsu K., Takada M., Li Y., 2017, *Phys. Rev. D*, **95**, 083522
- Akitsu K., Sugiyama N. S., Shiraiishi M., 2019, *Phys. Rev. D*, **100**, 103515
- Bagla J. S., 2002, *Journal of Astrophysics and Astronomy*, **23**, 185
- Baldauf T., Seljak U., Senatore L., Zaldarriaga M., 2011, *J. Cosmology Astropart. Phys.*, **2011**, 031
- Baldauf T., Seljak U., Desjacques V., McDonald P., 2012, *Phys. Rev. D*, **86**, 083540
- Baldauf T., Seljak U., Senatore L., Zaldarriaga M., 2016, *J. Cosmology Astropart. Phys.*, **2016**, 007
- Barreira A., Schmidt F., 2017, *J. Cosmology Astropart. Phys.*, **2017**, 053
- Barreira A., Krause E., Schmidt F., 2018, *J. Cosmology Astropart. Phys.*, **2018**, 015
- Barreira A., Nelson D., Pillepich A., Springel V., Schmidt F., Pakmor R., Hernquist L., Vogelsberger M., 2019, *MNRAS*, **488**, 2079
- Bode P., Ostriker J. P., Xu G., 2000, *ApJS*, **128**, 561
- Bond J. R., Myers S. T., 1996, *ApJS*, **103**, 1
- Chisari N. E., Dvorkin C., Schmidt F., Spergel D. N., 2016, *Phys. Rev. D*, **94**, 123507
- Crocce M., Pueblas S., Scoccimarro R., 2006, *Mon. Not. Roy. Astron. Soc.*, **373**, 369
- D'Aloisio A., McQuinn M., Trac H., Cain C., Mesinger A., 2020, arXiv e-prints, p. [arXiv:2002.02467](https://arxiv.org/abs/2002.02467)
- Dai L., Pajer E., Schmidt F., 2015, *J. Cosmology Astropart. Phys.*, **2015**, 059
- Dodelson S., 2003, *Modern cosmology*
- Gnedin N. Y., Kravtsov A. V., Rudd D. H., 2011, *ApJS*, **194**, 46
- Hamilton A. J. S., Rimes C. D., Scoccimarro R., 2006, *MNRAS*, **371**, 1188
- Heitmann K., et al., 2016, *ApJ*, **820**, 108
- Ip H. Y., Schmidt F., 2017, *J. Cosmology Astropart. Phys.*, **2017**, 025
- Kayo I., Takada M., Jain B., 2013, *MNRAS*, **429**, 344
- Laureijs R., et al., 2011, preprint, ([arXiv:1110.3193](https://arxiv.org/abs/1110.3193))
- Lawrence E., et al., 2017, *ApJ*, **847**, 50
- Lewis A., Challinor A., Lasenby A., 2000, *Astrophys. J.*, **538**, 473
- Li Y., Hu W., Takada M., 2014a, *Phys. Rev. D*, **89**, 083519
- Li Y., Hu W., Takada M., 2014b, *Phys. Rev. D*, **90**, 103530
- Li Y., Schmittfull M., Seljak U., 2018, *J. Cosmology Astropart. Phys.*, **2018**, 022
- Mohammed I., Martizzi D., Teyssier R., Amara A., 2014, preprint, ([arXiv:1410.6826](https://arxiv.org/abs/1410.6826))
- Moradinezhad Dizgah A., Dvorkin C., 2018, *J. Cosmology Astropart. Phys.*, **2018**, 010
- Nishimichi T., et al., 2009, *Publ. Astron. Soc. Japan*, **61**, 321
- Nishimichi T., et al., 2019, *ApJ*, **884**, 29
- Okumura T., Taruya A., 2020, *MNRAS*, **493**, L124
- Okumura T., Nishimichi T., Umetsu K., Osato K., 2018, *Phys. Rev. D*, **98**, 023523
- Osato K., Nishimichi T., Oguri M., Takada M., Okumura T., 2018, *MNRAS*, **477**, 2141
- Peebles P. J. E., 1980, *The large-scale structure of the universe*
- Planck Collaboration et al., 2016, *A&A*, **594**, A13
- Quinn T., Katz N., Stadel J., Lake G., 1997, arXiv e-prints, pp [astro-ph/9710043](https://arxiv.org/abs/hep-th/9710043)
- Sato M., Hamana T., Takahashi R., Takada M., Yoshida N., Matsumura T., Sugiyama N., 2009, *Astrophysical J.*, **701**, 945
- Schmidt F., Jeong D., 2012, *Phys. Rev. D*, **86**, 083513
- Schmidt F., Chisari N. E., Dvorkin C., 2015, *J. Cosmology Astropart. Phys.*, **2015**, 032
- Schmidt A. S., White S. D. M., Schmidt F., Stücker J., 2018, *MNRAS*, **479**, 162
- Scoccimarro R., 1998, *Mon. Not. Roy. Astron. Soc.*, **299**, 1097
- Sherwin B. D., Zaldarriaga M., 2012, *Phys. Rev. D*, **85**, 103523
- Sirko E., 2005, *ApJ*, **634**, 728
- Spergel D., et al., 2015, arXiv e-prints, p. [arXiv:1503.03757](https://arxiv.org/abs/1503.03757)
- Springel V., 2005, *Mon. Not. Roy. Astron. Soc.*, **364**, 1105
- Springel V., Yoshida N., White S. D. M., 2001, *New Astron.*, **6**, 79
- Stücker J., Schmidt A. S., White S. D. M., Schmidt F., Hahn O., 2020, arXiv e-prints, p. [arXiv:2003.06427](https://arxiv.org/abs/2003.06427)
- Sunayama T., et al., 2020, arXiv e-prints, p. [arXiv:2002.03867](https://arxiv.org/abs/2002.03867)
- Takada M., Hu W., 2013, *Phys. Rev. D*, **87**, 123504
- Takada M., Jain B., 2009, *MNRAS*, **395**, 2065
- Takada M., et al., 2014, *PASJ*, **66**, R1
- Takahashi R., Nishimichi T., Takada M., Shirasaki M., Shiroyama K., 2019, *MNRAS*, **482**, 4253
- Taruya A., Okumura T., 2020, *ApJ*, **891**, L42
- Wadekar D., Scoccimarro R., 2019, arXiv e-prints, p. [arXiv:1910.02914](https://arxiv.org/abs/1910.02914)
- Wagner C., Schmidt F., Chiang C. T., Komatsu E., 2015a, *MNRAS*, **448**, L11
- Wagner C., Schmidt F., Chiang C.-T., Komatsu E., 2015b, *J. Cosmology Astropart. Phys.*, **2015**, 042
- Xu G., 1995, *ApJS*, **98**, 355
- Zel'dovich Y. B., 1970, *A&A*, **5**, 84

This paper has been typeset from a $\text{\TeX}/\text{\LaTeX}$ file prepared by the author.